Supplementary Material for "Stiffness can mediate balance between hydrodynamic forces and avidity to impact the targeting of flexible polymeric nanoparticles in flow"

S. Farokhirad[1], A. Ranganathan[2], J. Myerson[3], V. R. Muzykantov[3,4], P. S. Ayyaswamy[1], D. M. Eckmann[2,5], and R. Radhakrishnan[5,6,7,*]
[1]*Department of Mechanical Engineering and Applied Mechanics*
[2]*Department of Anesthesiology and Critical Care*
[3]*Center for Targeted Therapeutics and Translational Nanomedicine, Institute for Translational Medicine & Therapeutics and Department of Pharmacology*
[4]*Translational Research Center*
[5]*Department of Bioengineering*
[6]*Department of Biochemistry and Biophysics*
[7]*Department of Chemical and Biomolecular Engineering University of Pennsylvania, Philadelphia, PA, 19104, USA*
(Dated: March 13, 2019)

S1 Details of the numerical methods

S1.1 Brownian Interactions

Core-Shell Cross-linked Polymer NP Model

We model the polymer microstructure as a fixed number of strands attached to a core, which mimics the experimentally inferred architecture for this material, where each strand is modeled as connected segments of freely jointed chains (FJCs). The core radius is set to $a = 10$ nm following the experimental estimates of [1]. We set the size of each bead in the arms to be the same as that of the core, i.e., $a = 10$ nm. The initial microstructure is a unit star polymer with 25 arms attached to a core, with each arm modeled by beads connected through four links in series; that is, each link connecting two adjacent beads in an arm is modeled as a Kuhn spring. The model is identical and is adopted from the work of Sarkar *et. al.* [2], where the stiffness of each link and the equilibrium distance is determined using a freely jointed chain model. The molecular weight of a dextran monomer is 162 Da and for a typical molecular weight of 70 kDa of the dextran polymer used to synthesize the NP, the number of monomers per arm is $\frac{70{,}000}{162}$ and the number of monomers per bead is $N = \frac{70{,}000}{4\times162}$. If the number of Kuhn's segments per bead is N_k and size of each Kuhn's segment is b_k, we impose $N_k b_k = Nb$, where b is the size of each monomer. For dextran, b_k is 0.44 nm and the size of the monomer (b) is 1.5 nm using which we calculate the stiffness (k_s) of the links between beads as derived from the FJC model, i.e., $k_s = \frac{3k_BT}{N_k b_k^2}$. We also model the stiffness of the coarse-grained crosslinks to be identical to the stiffness of each link. We mimic the experimental protocol to obtain a relaxed structure of the polymer assembly; details are available in [2]. For each NP stiffness we model $4-5$ configurations (replicas) and then carry out Brownian dynamics simulations as described below in each of the replicas. The error bars of the reported quantities are determined through the standard deviations of the five replicas.

The equations of motion of a system of connected beads with mass of m, radius of a and velocity of $\mathbf{v}$ are solved in a fluid with velocity $\mathbf{v}_o = \dot{\mathbf{r}}$ and viscosity μ, and the resulting force balance for one bead is given by,

$$m\frac{\mathrm{d}\mathbf{v}}{\mathrm{v}t} + 6\pi\mu a\left(\mathbf{v} - \dot{\mathbf{r}}\right) = \mathbf{F}^{\mathrm{br}} + \mathbf{F}^{\mathrm{nbr}}. \tag{1}$$

Here, $\dot{\mathbf{r}} = \mathbf{r}\cdot\nabla\mathbf{u}$ ($\nabla\mathbf{u}$ represents the velocity gradient from external forces), $\mathbf{F}^{\mathrm{br}}$ represents Brownian forces and $\mathbf{F}^{\mathrm{nbr}}$ is non-Brownian (deterministic) forces due to inter-bead interactions, due to margination, due to glycocalyx layer, and due to NP-cell adhesion. We consider time scales larger than inertial relaxation time (i.e., $\frac{m}{6\pi\mu a}$). Following Ermak and McCammon [3] we reduce Eq. (1) for time greater than time scale of internal relaxation (i.e., $t \gg \frac{m}{\xi}$) to:

$$\Delta\mathbf{r}_i = \dot{\mathbf{r}}_i\Delta t + \frac{1}{\xi}\left(\mathbf{F}_i^{\mathrm{br}} + \mathbf{F}_i^{\mathrm{nbr}}\right)\Delta t, \tag{2}$$

where $\xi = 6\pi\mu a$ is the friction factor and $\mathbf{r}_i$ and $\mathbf{F}_i$ denote the position and force associated with particle i, respectively. The Brownian forces are determined by diagonalizing the mobility tensor. We consider unconstrained Brownian forces

that are δ-correlated and represented as a white noise process between time t and $t + \Delta t$:

$$\langle \mathbf{F}^{i}_{\mathrm{br}}(t) \rangle = \mathbf{0} \tag{3}$$

$$\langle \mathbf{F}^{i,\mathrm{br}}(t) \mathbf{F}^{j,\mathrm{br}}(t') \rangle = 2k_{\mathrm{B}}T\xi\delta_{ij}\delta(t-t')\mathbf{I}. \tag{4}$$

Here, i and j are indices representing particular beads, k_{B} is the Boltzmann's constant, T is temperature, $\mathbf{I}$ is the unit second-order tensor, and $\delta(t-t')$ is the Dirac delta function. We scale time t with relaxation time of diffusion $\frac{a^2}{D_o}$ (where D_o is the unconstrained diffusivity of a Brownian particle which is $\frac{k_{\mathrm{B}}T}{\xi}$), r with a, and F with $\frac{k_{\mathrm{B}}T}{a}$.

Bead-to-bead hydrodynamic interactions

The hydrodynamic mobility tensor is described by adopting the Ronte-Prager-Yamakawa tensor [4, 5] to introduce the effect of bead-to-bead hydrodynamic interactions:

$$\begin{aligned}
\mathbf{M}^{HI,ij} =& \frac{1}{6\pi\mu a}\vec{I} \text{ for } i = j \ , \\
=& \frac{1}{8\pi\mu r}\left[\left(1+\frac{2a^2}{3r^2}\right)\mathbf{I} + \left(1-\frac{2a^2}{r^2}\right)\frac{\mathbf{rr}}{r^2}\right] \text{ for } i \neq j, r \geq \sigma \ , \\
=& \frac{1}{6\pi\mu a}\left[\left(1-\frac{9r}{32a}\right)\mathbf{I} + \frac{3r}{32a}\frac{\mathbf{rr}}{r^2}\right] \text{ for } i \neq j, r < \sigma \ ,
\end{aligned} \tag{5}$$

where i and j are indices of a pair of beads and σ is the interparticle distance ($\sigma = 2a$). $\mathbf{r} = r^{ij}$ is the relative position vector between beads i and j, while $\frac{\mathbf{rr}}{r^2}$ is the product of normalized vectors. Because of the long range of the mobility tensor, i.e., $r \gg a$, Eq. (5) decays slowly as $\frac{1}{r}$.

Effect of wall-mediated interactions

Near the endothelial surface the beads exhibit an anisotropic hindered Brownian motion due to hydrodynamic effects. The modified diffusion coefficient, in the directions parallel and normal to the surface, is expressed in terms of their respective mobilities. The NP exerts a force on the Newtonian solvent due to bead motions. We account for the effect of hydrodynamic interactions on the NP near a wall via decreased mobility of beads of the NP and increased drag due to the presence of other NPs. The effect of the wall is translated to the self-mobility shown in Eq. (5). Faxen and Angew [6] showed that a spherical particle, moving parallel to a rigid planar wall, experiences a decrease in mobility by a factor:

$$\beta_{\parallel} = 1 - \frac{9}{16}\left(\frac{a}{y}\right) + \frac{1}{8}\left(\frac{a}{y}\right)^3 - \frac{45}{256}\left(\frac{a}{y}\right)^4 - \frac{1}{16}\left(\frac{a}{y}\right)^5 \tag{6}$$

where, $\frac{a}{y} > 2$. For the present case due to repulsion from the wall and glycocalyx layer, the distance between beads and the wall will be always larger than $2a$. Wakiya [7] showed that using the method of reflections as applied to two spherical particles in the presence of a planar wall, a spherical particle moving towards the wall experiences an increased drag which is given by:

$$\beta_{\perp} = 1 - \frac{9}{8}\left(\frac{a}{y}\right) + \frac{1}{2}\left(\frac{a}{y}\right)^3 - \frac{2}{8}\left(\frac{a}{y}\right)^5 . \tag{7}$$

It must be noted that in our simulations, the hydrodynamic interactions between one bead and the wall are taken into account through the use of Eqs. (6) and (7) and the simultaneous effect of HI between multiple beads and the wall is presently ignored, as the size of the bead is smaller than the instantaneous distance of its center from the wall.

Effect of concentration

Effects of the presence of other NPs are considered by including interactions of the periodic images through the Ewald sum method described by Beenakker [8]. The resultant velocity is a product of the overall mobility from the

Ewald sum and the forces acting on the bead, i.e.:

$$\mathbf{v}^i = \sum_{j=1}^{N} \sum_{\mathbf{l}} \mathbf{M}^{\mathrm{HI},ij}\left(\mathbf{r}_{\mathbf{l}}^{ij}\right) \cdot \mathbf{F}^j, \tag{8}$$

where $\mathbf{r}_l^{ij}$ is the distance between the periodic images of the box and $\mathbf{l}$ is comprised of components of two dimensional lattice vectors expressed as $\mathbf{l} = (l_1 L, l_2 L)$ and L is the length of the simulation box.

To include the effect of other beads in the mobility of a test bead, we adopt a quasi-2D Ewald sum of the mobility tensor shown by Bleibel [9]. The pair-wise mobility tensor is then defined by:

$$\begin{aligned} 6\pi\mu a \mathbf{v}^i =& 6\pi\mu a \sum_{j=1}^{N} \mathbf{M}^{\mathrm{HI},ij}\left(\mathbf{r}^{ij}\right) \cdot \mathbf{F}^j \\ &+ \left(1 - \frac{3}{2}\pi^{-1/2} a\alpha - \frac{2}{3}\pi^{-1/2} a^3 \alpha^3\right) \mathbf{F}^i \\ &+ \sum_{\substack{\mathbf{l} \\ (l \neq 0)}} \sum_{j=1}^{N} \mathbf{M}^{(1)}\left(\mathbf{r}^{ij} + \mathbf{l}\right) \cdot \mathbf{F}^j \\ &+ \frac{1}{V} \sum_{\substack{k \\ \mathbf{k} \neq 0}} \sum_{j=1}^{N} \mathbf{M}^{(2)}\left(\mathbf{k}\right) \cos\left(\mathbf{k} \cdot \mathbf{r}^{ij}\right) \cdot \mathbf{F}^j, \end{aligned} \tag{9}$$

where $\mathbf{M}^{(1)}$ & $\mathbf{M}^{(2)}$ are contributions from periodic images along '1' and '2' directions and are defined in [9]. We numerically check the convergence of the mobility tensors to determine the number of boxes and the value of convergence parameter α. The mobility tensor converges for 25 periodic boxes with $\alpha = 0.125/a$.

S1.2 Non-Brownian Interactions

In addition to Brownian forces, the beads experience some non-Brownian forces. The illustration shown in Fig. 1 highlights the major components of the forces due to non-Brownian interactions, which will be described in the following sections.

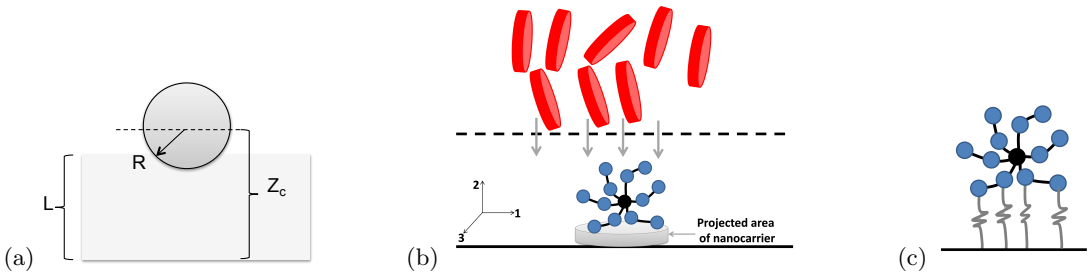

FIG. 1: Schematic of (a) the NP bead near a glycocalyx layer, (b) deformable NP under margination potential from red blood cells (RBCs), (c) deformable NP tethered to endothelial surface.

Glycocalyx mediated interaction of NP with endothelial cells

NP adhesion is subject to glycocalyx resistance and influenced by flexural rigidity of receptors and receptor-ligand bond stiffness. The glycocalyx has a significant role in modulating NP binding to endothelial cells by imposing an energy barrier. We employ an equilibrium model to determine the force acting on each bead due to glycocalyx mediated interaction of functionalized NP with endothelial cells [10]. Fig. 1(a) shows a bead of the NP immersed in the glycocalyx layer. Following Agrawal and Radhakrishnan [10], the resistance offered by the glycocalyx on each

bead is defined by a harmonic energy of interaction. The ensuing force exerted by the glycocalyx layer on the bead is obtained as the negative gradient of the energy of interaction along the perpendicular direction:

$$F_{\mathrm{glyx}} = -\frac{\mathrm{d}E_{\mathrm{glyx}}}{\mathrm{d}y} = \pi k_{\mathrm{glyx}} a^3 \left[\frac{L_{\mathrm{glyx}} - y}{a} + 1\right]^2 . \tag{10}$$

E_{glyx} is energy of interaction, y is the perpendicular coordinate of the center of the bead, L_{glyx} is the thickness of the glycocalyx, and k_{glyx} is the glycocalyx stiffness.

Margination of NP by RBC

Larger particulates in suspension such as RBCs can modulate carrier interactions with the endothelium. We adopt the DDFT approach introduced by Yu *et al.* [11] to include the effect of inertial margination due to flow on the spheres as shown in Fig. 1(b). Two different ensemble averages, i.e., the grand canonical (μVT) and the canonical (NVT) ensembles, were considered in [11] to represents conditions common in experiments. If the chemical potential is controlled in the equilibrium state, the grand canonical ensemble is used, whereas the canonical ensemble is invoked when the numbers of particulates are held fixed, depending on the physical system. The flow profiles are considered to be parabolic for dilute suspensions and a blunted parabolic for denser suspensions. In both ensembles, the expression for the mean-field DDFT equation in the presence of convective flow and external potentials is defined as:

$$\frac{\partial \rho^{\mathrm{RBC}}(\mathbf{r},t)}{\partial t} + \nabla \cdot \rho^{\mathrm{RBC}}(\mathbf{r},t) \left\langle \mathbf{v}_1 \right\rangle_1 = \nabla \cdot \frac{\langle D_s \rangle_1}{k_{\mathrm{B}}T} \cdot \rho^{\mathrm{RBC}}(\mathbf{r},t) \nabla \frac{\delta F[\rho^{\mathrm{RBC}}(\mathbf{r},t)]}{\delta \rho^{\mathrm{RBC}}(\mathbf{r},t)}, \tag{11}$$

where, $\langle\rangle_1$ denotes a conditional average with the position of one particle held fixed, $\mathbf{v}_1$ is the velocity of the chosen particle, D_s is the self-diffusivity tensor for a particle and F is the Helmholtz free energy defined as a function of the one-body particle density, i.e., $F[\rho^{\mathrm{RBC}}(\mathbf{r},t)] = F^{\mathrm{id}}[\rho^{\mathrm{RBC}}(\mathbf{r},t)] + F^{\mathrm{ex}}[\rho^{\mathrm{RBC}}(\mathbf{r},t)] + \int_V U_{\mathrm{ext}}(\mathbf{r},t)\rho^{\mathrm{RBC}}(\mathbf{r},t)$. Here, F^{id} is the ideal gas free energy, i.e., $F^{\mathrm{id}} = k_{\mathrm{B}}T \int_V \rho^{\mathrm{RBC}}(\mathbf{r},t)[\ln(\rho^{\mathrm{RBC}}(\mathbf{r},t)\Lambda^3) - 1]d\mathbf{r}$ with Λ being the thermal de Broglie wavelength of the particle, U_{ext} is the external potential energy, and F^{ex} denotes the excess Helmholtz free energy.

Considering the steady-state behavior of the system, the DDFT equation for $\rho^{\mathrm{RBC}}(\mathbf{r})$ under fixed particle number condition is expressed as:

$$\rho^{\mathrm{RBC}}(r) = \rho_{\mathrm{b}} \exp\left\{-\frac{1}{k_{\mathrm{B}}T}\frac{\delta F^{\mathrm{ex}}[\rho^{\mathrm{RBC}}(r)]}{\delta \rho^{\mathrm{RBC}}(r)} + \frac{1}{k_{\mathrm{B}}T}\frac{\delta F^{\mathrm{ex}}(\rho_{\mathrm{b}})}{\delta \rho_{\mathrm{b}}} - \frac{U_{\mathrm{ext}}(r)}{k_{\mathrm{B}}T} + \int_0^r \frac{f_{\mathrm{lift}}(r')}{k_{\mathrm{B}}T}\mathrm{d}r'\right\}, \tag{12}$$

where, ρ_{b} is the particle number density in the bulk and f_{lift} is the lift force acting on a chosen particle. The margination potential felt by each bead of the NP at every position r' is defined as:

$$\Phi^{\mathrm{RBC}}(r') = \int_V \rho^{\mathrm{RBC}}(r)\langle\phi(r',r)\rangle \mathrm{d}r, \tag{13}$$

where ρ^{RBC} is the density of RBCs at some distance r and ϕ represents the interaction of a given spherical particle with RBCs using the following Weeks-Chandler-Andersen (WCA) type potential:

$$\phi(r,r') = 4\epsilon\left[\left(\frac{\sigma}{r-r'}\right)^{12} - \left(\frac{\sigma}{r-r'}\right)^{6} + \frac{1}{4}\right]. \tag{14}$$

Here, $\epsilon = 0.7k_{\mathrm{B}}T$ and $\sigma = \frac{a+b}{2}$ with b being the radius of RBC, denote the energy and length units, respectively. The margination potential defined in Eq. (13) comes from hydrodyanmic origin at the steady-state as clearly demonstrated in [11] in the DDFT approach. The force due to margination, i.e., $F^{\mathrm{marg}} = -\nabla\Phi^{\mathrm{RBC}}$ is stochastically exerted by passing RBCs, which migrate to the axis of flow and varies with distance from the wall. We include the margination force on the NP, based on the NP effective radius, as an external non-Brownian force term.

Finally the lift force felt by a given spherical NP with radius of r_s in the region of the parabolic flow of length L is determined by Yu *et al.* [11]:

$$\frac{F_{\mathrm{lift}}(y)}{k_{\mathrm{B}}T} = RePe\beta_{\perp}\frac{5}{288}\left(\frac{r_s}{L^2}\right)\left(1 - \frac{y}{L}\right)\left(22 - 73\frac{y}{L}\right). \tag{15}$$

Here, $RePe$ is product of the Reynolds number and Peclet number, and $\beta_{\perp}$ denotes the wall-induced resistivity factor, see Eq. (7).

Inter-bead interactions and adhesion of functionalized NP to the cell surface

Agrawal and Radhakrishnan [10] have proposed a computational model for NP adhesion to endothelial cells and compared predictions with experimentally measured binding parameters using molecular and energetic analyses to quantify the NP binding process. Following Sarkar *et al.* [2], the interaction between adjacent connected beads is considered through a harmonic potential:

$$U^{\mathrm{s}} = \frac{1}{2}k^{\mathrm{s}}\left(r - r_o\right)^2, \tag{16}$$

where, r_o is the equilibrium bond distance and is set to $2a$. The spring restoring forces (F^{s}) are derived by taking the spatial derivative of the segmental chain free energy.

Excluded volume effects of the beads are considered as a purely repulsive WCA potential [12]:

$$U^{\mathrm{WCA}} = 4\epsilon\left[\left(\frac{\sigma}{r}\right)^{12} - \left(\frac{\sigma}{r}\right)^{6} + \frac{1}{4}\right]. \tag{17}$$

Here, $\frac{\epsilon}{k_{\mathrm{B}}T}$ is the scaled interaction strength with $\epsilon = 0.7k_{\mathrm{B}}T$ and σ is the excluded volume radius. The cut-off radius for WCA potential is set to $r_C = 2^{\frac{1}{6}}\sigma$.

Anti-ICAM (antibody specific for ICAM-1) functionalized NPs bind to target antigens on the cell surface. We model the binding of each bead of a deformable NP coated with antibody as a detachable spring that is connected to the ICAM-1 receptors diffusing on the surface. Despite being a coarse-grained model, the molecular nature of the receptor-ligand interactions is retained, which allows us to precisely compute the entropic contributions to binding efficacy , as well as to gauge how the ability of antibodies to bind to the antigens is modulated by molecular flexure, see [13] for details. The binding interaction between a ligand i and a receptor j is defined using the Bell potential:

$$U^{\mathrm{Bell}}(d^{ij}) = \frac{1}{2}k^{\mathrm{eff}}\left(d^{ij} - d^*\right)^2, \tag{18}$$

for $d^{ij} \leq d^*$ and 0 for $d^{ij} \geq d^*$. Here, d^{ij} is the distance between the tip of the chosen receptor and the center of the bead supporting the ligand and d^* is the cutoff distance for binding interaction. $d^* = a + d_o$, where d_o is the length of the antiICAM molecule. In the description above, the effective spring constant is given by a combination of the molecular stiffness surrounding the receptor-ligand bond [13, 14] and that of the polymer segment represented by a bead. That is $k_{\mathrm{eff}} = \frac{k^{\mathrm{s}} \times k^{\mathrm{ICAM-antiICAM}}}{k^{\mathrm{s}} + k^{\mathrm{ICAM-antiICAM}}}$ with $k^{\mathrm{ICAM-antiICAM}} \simeq 1$ N/m being the spring constant of a receptor-ligand bond.

Brownian Dynamics (BD)

In the BD method, we include the inhomogeneous nature of the system due to wall effects by considering the distance dependent changes to the mobility. Following Ermak and McCammon [3] we introduce a drift velocity given by $\frac{\partial D_2^i}{\partial r_2^i}$ along the perpendicular direction 2.

We modify Eq. (1) using the mobility tensor shown in Eq. (5). We include all non-hydrodynamic forces such as spring restoring force ($\mathbf{F}_i^{\mathrm{s}}$), force due to excluded volume effect ($\mathbf{F}_i^{\mathrm{WCA}}$), force due to NP adhesion to the cell surface ($\mathbf{F}_i^{\mathrm{adh}}$), force due to glycocalyx layer ($\mathbf{F}_i^{\mathrm{glyx}}$), and force due to margination of RBCs ($\mathbf{F}_i^{\mathrm{RBC}}$). The displacement due to Brownian movement is weighted with the resultant diffusion tensor obtained from the Rotne-Prager-Yamakawa (RPY) tensor and is given by:

$$\frac{\Delta \mathbf{r}_i}{\Delta t} = \mathbf{M} \cdot \left(\mathbf{F}_i^{\mathrm{WCA}} + \mathbf{F}_i^{\mathrm{s}} + \mathbf{F}_i^{\mathrm{adh}} + \mathbf{F}_i^{\mathrm{glyx}} + \mathbf{F}_i^{\mathrm{RBC}}\right) + \sqrt{2}\mathbf{B} \cdot d\mathbf{W}. \tag{19}$$

Here, $\mathbf{W}$ represents the matrix of values of a Gaussian stochastic process with zero mean and unit variance, and $\mathbf{B}$ is a weight factor which is calculated from $\mathbf{M}$ using:

$$\mathbf{M} = \mathbf{B} \cdot \mathbf{B}^T. \tag{20}$$

We follow the Cholesky decomposition of the Rotne-Prager-Yamakawa tensor to compute $\mathbf{B}$. Since the Rotne-Prager-Yamakawa tensor is positive definite, the Cholesky decomposition is numerically stable. The details of the

TABLE I: Details of the coarse-grained model of NP

Property	Symbol	Value
Number of cores	N_{c}	1
Bead radius	a	10 nm
Number of beads in an arm	N_{b}	4
Arms attached to a core	f	25
Molecular weight of Dextran monomer	M_{monomer}	160 Da
Molecular weight of Dextran polymer	M_{polymer}	71 kDa
Size of each Kuhn segment	b_{k}	0.44 nm
Size of monomer	b	1.5 nm
Number of monomers per bead	N	108
Number of Kuhn segments	N_{k}	368
Stiffness of spring between beads	k_{s}	$1.74329\times10^{-4}\,\frac{\mathrm{J}}{\mathrm{m}^2}$
Glycocalyx height	L_{glyx}	100 nm
Glycocalyx stiffness	k_{glyx}	$3.9\times10^{9}\,\frac{\mathrm{J}}{\mathrm{m}^4}$
antigen length	L_{ant}	19 nm
antibody length	L_{ab}	15 nm
number of antigens	N_{ant}	2000
number of antibodies per NP	N_{ab}	162
system temperature	T	300 K

model and methods are given in [2]. The bond stiffness for cross-links are kept the same as that of the stiffness of the inter bead springs. We report the number of cross-links as a percentage based on the number of bonds. The detailed parameter sets used in our model are summarized in Table I. It must be noted that in the calculation of the margination potential due to to blood particulates such as RBCs, the hydrodynamic interactions between RBCs and individual bead can be taken into account explicitly at the RPY level [15].

S1.3 Analysis of simulation

Diffusivity, Radius of gyration and shape of NP

We compute the radius of gyration based on bead positions. [2] showed that, when there is no confinement effect, the radius of gyration of the polyemric NP decreases with increasing the NP stiffness. The NP at a distance $h \gg \mathcal{O}(a)$ (from the wall) is not effected by any other forces. To test our hypothesis we compute eigenvalues of the radius of gyration matrix which is defined in terms of bead positions:

$$\mathbf{G} = \frac{1}{N}\sum_{i=1}^{N}\left(\mathbf{r}^i - \mathbf{r}^{\mathrm{cm}}\right)\left(\mathbf{r}^i - \mathbf{r}^{\mathrm{cm}}\right), \tag{21}$$

where *cm* denotes center of mass of the NP. Eigenvalues (λ_i $(i = 1, 3)$) of $\mathbf{G}$ denote the characteristic size along three orthogonal directions. The radius of gyration is then defined as:

$$R_{\mathrm{g}}^2 = \sum_{\mathrm{m}=1}^{3}\lambda_{\mathrm{m}}. \tag{22}$$

We further compute the shape of the NP, given by:

$$S = \frac{27\langle\prod_i^3\left(\lambda_i - \bar{\lambda}\right)\rangle}{\langle\left(\sum_i^3\lambda_i\right)^3\rangle}, \tag{23}$$

where $\bar{\lambda} = \frac{1}{3}\left(\sum_i^3\lambda_i\right)$. Bishop and Michels [16] have showed that S varies from -0.25 to 2, where the change in sign from '-ve' to '+ve' signifies an oblate to a prolate shape change.

Structure factor

The eigenvalues of the radius of gyration tensor provide information on the shape of the NP. To quantify the structure of the NP, we compute the structure factor, defined as:

$$S(\mathbf{k}) = \langle \frac{1}{N} \left| \sum_{j=1}^{N} \exp\left(-i\mathbf{k}\cdot\mathbf{r}^j\right) \right|^2 \rangle, \tag{24}$$

where $\mathbf{k}$ is the wave vector, $\mathbf{r}^j$ represents the position of bead j, and the average represents an average over the trajectory. Typically, we choose $\mathbf{k} = (k, 0, 0)$ and plot $S(k)$ against k_1. The $S(k_1)$ at large k_1 provides information about NP internal structure, while $S(k_1)$ at the small k_1 characterizes the overall packing of NPs.

Configurational entropy using quasi-harmonic analysis

Following Carlsson and Aqvist [17] and Balsera *et al.* [18], we compute the configurational entropy using a principal component analysis of the covariance matrix associated with coordinate fluctuations. In the analysis, the fluctuations about orthogonal degrees of freedom of the beads are treated as being generated by independent harmonic oscillators and the thermodynamic conformational entropy is calculated as a sum of these independent harmonic oscillators. The covariance matrix of the $3N$ Cartesian coordinates with N being the number of beads of the NP is given by:

$$B_{ij} = \langle (r_i - \langle r_i \rangle)\,(r_j - \langle r_i \rangle) \rangle\,. \tag{25}$$

Here B_{ij} is the symmetric covariance matrix, r_i represents the coordinate of the ith degree of freedom, where $i = 1, ..., 3N$. In these calculations, three eigenvalues (≈ 0) correspond to translation about the center of mass, three eigenvalues (≈ 0) correspond to rotation about center of mass, and the remaining $3N - 6$ correspond to vibrational motions. These frequencies about the principal directions are computed by solving the equation:

$$det\left(\mathbf{m}^{\frac{1}{2}}\mathbf{B}\mathbf{m}^{\frac{1}{2}} - \frac{k_B T}{\omega^2}\mathbf{I}\right) = 0. \tag{26}$$

Here, ω is the angular frequency and $\mathbf{m}$ is the mass matrix with the masses of the bead of NP on the diagonal and all off-diagonal elements equal to zero. The quasi-harmonic entropy is then calculated from the frequency obtained from Eq. (26) using the relationship:

$$S_{\mathrm{qh}} = k_{\mathrm{B}} \sum_i \left[\frac{\hbar\omega_i / k_{\mathrm{B}}T}{\exp(\hbar\omega_i / k_{\mathrm{B}}T) - 1} - \ln\left[1 - \exp(-\hbar\omega_i / k_{\mathrm{B}}T)\right] \right], \tag{27}$$

where $\hbar$ is the Planck's constant divided by 2π and ω_i is the set of angular frequencies obtained by solving Eq. (26).

The vibrational entropy of NP upon binding is computed from Eq. (27) where the eigen modes of internal vibrations are computed using a principal component analysis of the covariance matrix of configurational fluctuations captured in the BD trajectories (Eq. (25)). The covariance matrix for bead position fluctuations are corrected for removal of the translational and rotational movement contributions. A similar procedure is followed for conditions where the NP is away from the wall.

S1.4 Numerical solutions of the Fokker-Planck equation

We consider the steady-state behavior of the system and rewrite the Fokker-Planck equation, in terms of dimensionless variables:

$$A(y)\frac{d^2c}{dy^2} + B(y)\frac{dc}{dy} - E(y)c = 0. \tag{28}$$

where $A(y) = \beta_\perp$, $B(y) = \frac{dA(y)}{dy} - F(y)A(y)$, $E(y) = \frac{dA(y)}{dy}F(y) + A(y)\frac{dF(y)}{dy}$, and $F(y) = F_{\mathrm{lift}}(y) + F_{\mathrm{marg}}(y) + F_{\mathrm{glyx}}(y)$. Numerical solutions to the second-order partial differential equation with boundary conditions corresponding to a boundary value problem (i.e., Eq. (28)) are obtained using a finite difference method. By invoking the central

difference approximations for the concentration term we have reduced our ordinary differential equation for N number of nodes to a system of N algebraic equations which is given by

$$[A(y_n) - \frac{\Delta y}{2}B(y_n)]c_{n-1} - [2A(y_n) + \Delta y^2 E(y_n)]c_n + [A(y_n) + \frac{\Delta y}{2}B(y_n)]c_{n+1} = 0. \tag{29}$$

If a_{ij} is the i^{th} row and j^{th} column entry of a matrix with square coefficients, then the three non-zero diagonals along a row are:

$$a_{n,n-1} = A(y_n) - \frac{\Delta y}{2}B(y_n)\ , \tag{30}$$

$$a_{n,n} = -[2A(y_n) + \Delta y^2 E(y_n)]\ , \tag{31}$$

$$a_{n,n+1} = A(y_n) + \frac{\Delta y}{2}B(y_n), \tag{32}$$

while all other entries of a_{ij} are zero. To account for the boundary conditions, we have altered non-zero values of a_{ij} in the first and last rows of the matrix, one at y_1 and the other at y_{N}, by applying the following conditions:

$$\frac{dc}{dy}|_{y=y_1} = 0\ , \tag{33}$$

$$c(y_{\mathrm{N}}) = c_0. \tag{34}$$

The solutions are provided in Fig. 2.

S2 Details of the experiment

S2.1 NP characterization and targeting antibody loading

Fluorescein isothiocyanate (FITC) labeled polystyrene spheres (PS beads) of 200 nm diameter and non-labeled 8 μm PS beads were purchased from Polysciences (Warrington, PA). All other reagents were from Sigma Chemical (St. Louis, MO) unless otherwise mentioned. Rhodamine-dextran lysozyme polymeric NPs were synthesized using a method adopted from a previous study [19], described in short here: Rhodamine labeled Dextran from Leuconostoc ssp and Lysozyme were dissolved $(1:1)$ in water; pH of the solution was adjusted to $7-8$ using 0.1 N sodium hydroxide and was lyophilized. The lyophilized powder was spread out on a glass surface and kept in a desiccator containing saturated KBr solution to react at 60°C under 79% relative humidity for $18-24$ h. The reacted powder was reconstituted in water (5 mg/ml); the pH was adjusted to 10.7 (isoelectric point of lysozyme) using 0.1 N sodium hydroxide, and the solution was heated at 80°C for 30 min. Once synthesized, polymeric NPs were purified via centrifugation using Amicon Ultra-0.5 ml centrifugal filter devices with a 100 kDa molecular weight cutoff (Millipore, Billerica, MA), using the directions of the manufacturer (14000 g for 10 min to filter off free dextran and lysozyme and 1000 g for 2 min to recover retained polymeric NPs) to which an oxidizing agent (0.01 M NaIO4), 25 wt. percent NaCl and deionized water (to bring up volume to 1 mL) were added.

The NPs (PS beads and polymeric NPs) were characterized by dynamic light scattering using a ZS90 Malvern Zetasizer Nano Series instrument (Malvern, Westborough, MA). Antibody loading of the NPs was performed as has been previously published [20, 21]. Briefly, for polymeric NP Ab loading, the oxidation reaction (on the chains of the polymeric NP outer dextran shell) was placed on a shaker for 3 days after which oxidized polymeric NPs were purified using centrifugation and 100 μg anti-Intercellular Adhesion Molecule 1 (anti-ICAM-1) antibody R6.5 (derived in house from hybridoma) was added and allowed to react for about 24 hours on a shaker. PS beads were conjugated with R6.5 Ab by physisorption via incubation for 60 min. Free non-coated Ab was then separated by centrifugation, and coated PS beads were re-suspended in PBS supplemented with 1% BSA.

S2.2 Endothelial cell culture, flow adaptation and NP exposure during flow

ICAM-expressing Chinese hampster ovary cells i.e., CHO cells, purchased from Sigma-Aldrich were plated in RPMI 1640 (w/ 25 mM HEPES) supplemented with 10% Fetal Bovine Serum. Cell media samples were regularly checked for mycoplasma contamination using MycoAlert Kit (Lonza, Rockland, ME). For dynamic experiments, cells of passage

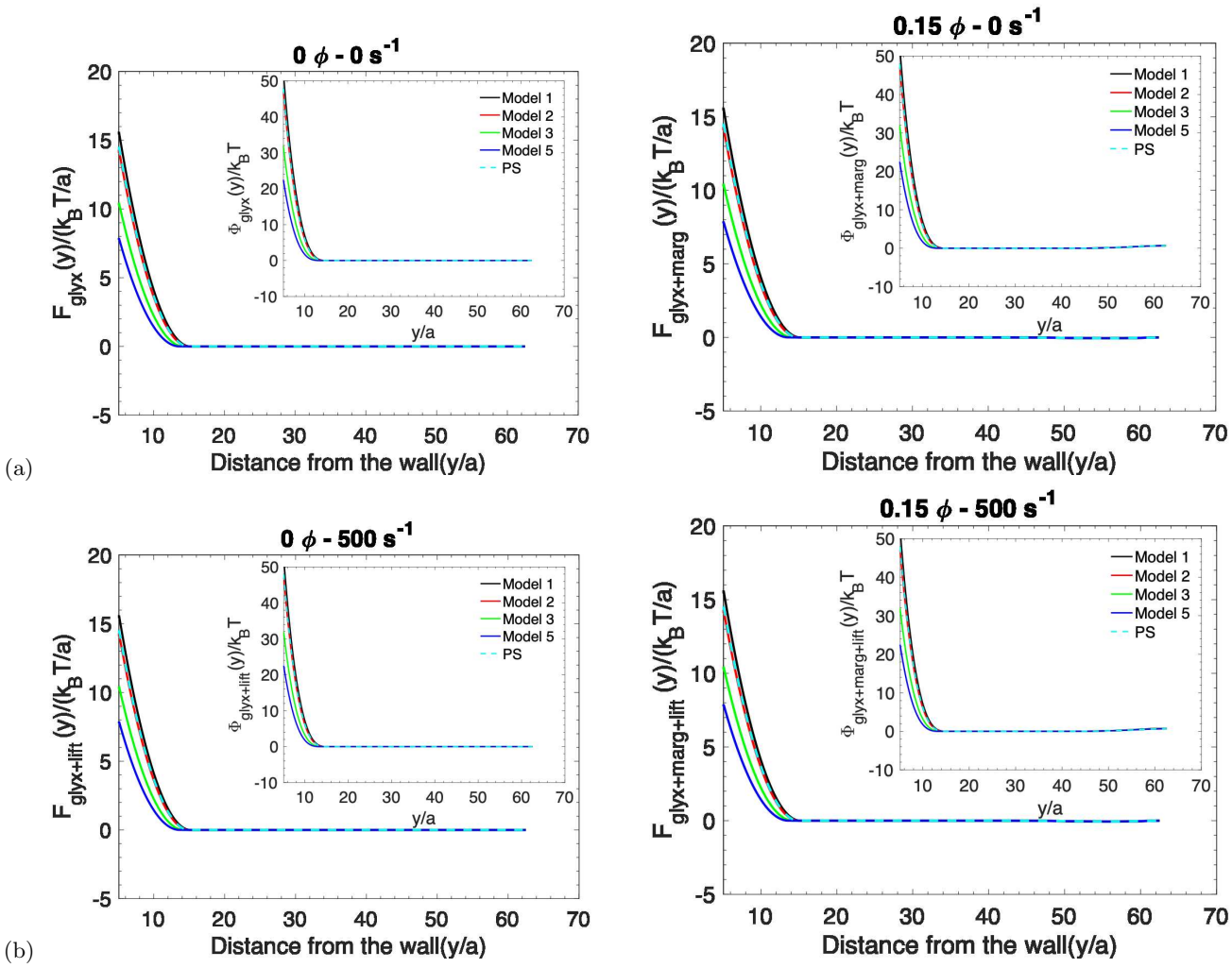

FIG. 2: Force due to contributions of shear flow and volume fraction of particulate suspension, i.e., ϕ. (a) 0 s^{-1} and (b) 500 s^{-1}. The inset shows the potential energy.

2 or 3 were plated onto 22X40 Fisherbrand microscope cover glass (Fisher Scientific, Pittsburgh, PA) with 1% m/v Gelatin.

Confluent cells were assembled into confocal imaging chambers (Warner Instruments, Hamden, CT) and flow adapted using a peristaltic pump for 4 hours to mimic endothelium whose actin fibers are aligned to flow as in the human microvasculature at shear stresses of 100 and 500 s^{-1}. NPs (192 nm polymeric NPs or 200 nm PS beads) were introduced into the perfusate for dynamic NP binding studies at a concentration of 7.6×10^{11}/ml. The 8μm PS beads were added to the perfusate in concentrations of 0, 0.1 and 0.3 of the perfusate volume to simulate the relevant physiological red blood cell volume fraction.

Imaging NP binding

Images for dynamic experiments were observed using an Olympus IX-51 and captured using Hamamatsu ORCA Flash 4.0 camera (Shizuoka, Japan) and a Luemncor LED light source (Beaverton, OR). Cells were imaged at 15, 60 and 240 min using a 40X Oil immersion lens (BioVision Technologies, Exton, PA). Images for each time point were averaged: 1-4 image frames per time point, per experiment and then group averaged over three experiments (all experiments were conducted in triplicates). Images taken for dynamic experiments were taken as a series of 10-15 frames.

Image analysis

Images obtained from the microscope (system was not image intensity saturated to obtain data) were processed on ImageJ before using MATLAB to count color pixels. Using the Triangle method (standard on ImageJ) of thresholding, particles were detected and extracted from the background eliminating noise. Each time point image had 15 frames, which were averaged to eliminate particles that were rolling and not firmly bound. Large aggregates captured in these averaged frames were then removed using a background subtracting function which excises all thresholded areas having a diameter more than that of the NP (this limit was set as 480 and 640 nm for polymeric NPs and PS beads respectively). The MATLAB program was used to provide fluorescence counts, which were normalized to cell number using cell counts performed on bright-field images obtained in sequence with the fluorescence images at each of the time-points. Finally we used the calibration method described in [22] to obtain an accurate count of the number of NPs bound per cell at each time point for each experimental condition. The results were scaled to the result for 200 nm PS bead binding at 15 min for 100 s^{-1} shear exposure.

Statistical analysis

ANOVA was performed on all data sets to determine significance. A p-value less than or equal to 0.05 was considered to be significant.

S2.3 In vivo targeting to vascular endothelium in mice

Anesthetized C57BL/6 female mice (16-24g, Harlan) were injected intravenously via jugular vein with NPs coated with murine anti-ICAM-1 (YN1 clone, Biolegend) or control rat IgG (Jackson Labs). The injected dose was $\sim 200\,\mu l$ (or ~ 10 mg/kg) with a tracer amount of antibody-coated ^{125}I-labeled NP. Blood was collected from the retro-orbital plexus at 30 min post-injection and organs (heart, kidneys, liver, spleen, and lungs) were collected at 30 min post-injection. Radioactivity and weight of the samples were determined to calculate polystyrene NP targeting. These studies were carried out in accordance with the Guide for the Care and Use of Laboratory Animals as adopted and promulgated by the U.S. National Institutes of Health. We quantified endothelial targeting as a function of lung uptake of NCs in mice. Lung uptake is representative of endothelial targeting because the lung accounts for roughly 30 % of the endothelium in vivo [23]. Moreover, previous works (see example [13]) indicate that only uptake in the pulmonary vasculature is dependent on the number of anti-ICAM molecules; thus we do not account for nontargeted tissues, because the uptake of particles in the main reticuloendothelial system (RES) organ, liver, did not change with variations of the anti-ICAM surface density. In fact, the hepatic uptake of any anti-ICAM/particle formulation was not different from that of IgG/particles. The same result, i.e., lack of significant difference in the uptake of various particle formulations, has been observed in the second main RES organ, spleen. Further, cardiac uptake of the particles, reflecting nonspecific uptake in the tissues other than RES, was the same for all particles regardless of the number of anti-ICAM molecules. The in vivo results for the polystyrene NP are depicted in Fig. 3(a).

In the case of polymeric NPs, NPs of 150 nm diameter were targeted to the endothelial surface protein ICAM (YN1 Ab) or the non-specific (IgG). Trace amounts of 125I-IgG enabled tracking. NPs were injected intravenously in mice (n=5 per group). Selected organs were removed and weighed prior to gamma counter detection of 125I to measure NP retention. NP biodistributions are reported in Fig. 3(b).

REFERENCES

[1] M. C. Coll Ferrer, R. C. Jr. Ferrier, D. M. Eckmann, and R. J. Composto, Journal of Nanoparticle Research **15**, 1-7 (2012) http://dx.doi.org/10.1007/s11051-012-1323-5.

[2] A. Sarkar, D. M. Eckmann, P. S. Ayyaswamy, and R. Radhakrishnan, Soft Matter **11**, 5955-5969 (2015) http://dx.doi.org/10.1039/C5SM00669D.

[3] D. L. Ermak, and J. A. McCammon, The Journal of Chemical Physics **69**(4), 1352-1360 (1978) http://dx.doi.org/10.1063/1.436761.

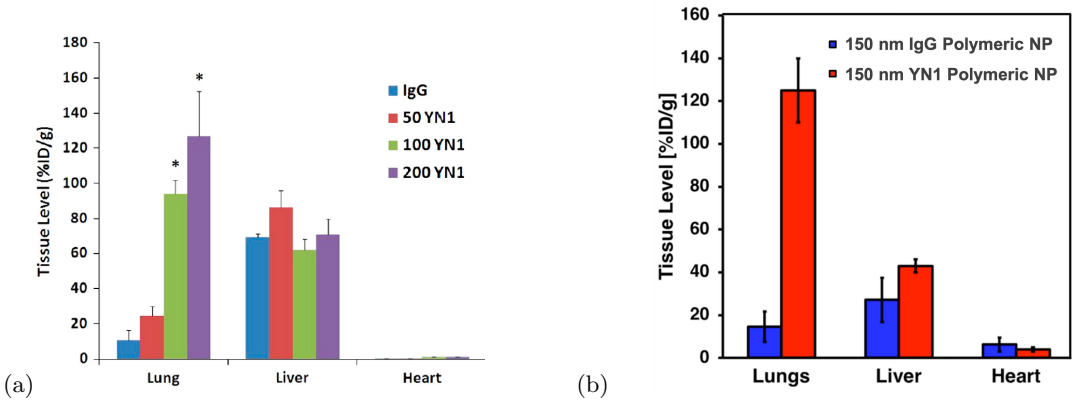

FIG. 3: The uptake of (a) PS and (b) polymeric NP in vivo.

[4] J. Rotne and S. Prager, The Journal of Chemical Physics **50**(11), 4831-4837 (1969) http://dx.doi.org/10.1063/1.1670977.

[5] H. Yamakawa, The Journal of Chemical Physics **53**(1), 436-443 (1970) http://dx.doi.org/10.1063/1.1673799.

[6] H. Faxen and Z. Angew, Math. Mech. **7**, 79-80 (1927).

[7] S. Wakiya, CJ. Phys. Soc. Japan **22**(4), 1101-1109 (1967) https://doi.org/10.1143/JPSJ.22.1101.

[8] C. W. J. Beenakker, The Journal of Chemical Physics **85**(3), 1581-1582 (1986) http://dx.doi.org/10.1063/1.451199.

[9] J. Bleibel, Journal of Physics A: Mathematical and Theoretical **45**(22), 225002 (2012) https://doi.org/10.1088/1751-8113/45/22/225002.

[10] N. J. Agrawal and R. Radhakrishnan, The Journal of Physical Chemistry C **111**(43), 15848-15856 (2007) http://dx.doi.org/10.1021/jp074514x.

[11] H. Y. Yu, Z. Jabeen, D. M. Eckmann, P. S. Ayyaswamy, and R. Radhakrishnan, Langmuir **33**(42), 11332-11344 (2017) http://pubs.acs.org/doi/abs/10.1021/acs.langmuir.7b01860.

[12] J. D. Weeks, D. Chandler, and H. C. Andersen, The Journal of Chemical Physics **54**(12), 5237-5247 (1971) https://doi.org/10.1063/1.451199.

[13] J. Liu, G. E. R. Gregory, B. Zern, P. S. Ayyaswamy, D. M. Eckmann, V. R. Muzykantov, and R. Radhakrishnan, Proceedings of the National Academy of Sciences **107**(38), 16530-16535 (2010) https://doi.org/10.1073/pnas.1006611107.

[14] M. McKenzie, S. M. Ha, A. Rammohan, R. Radhakrishnan, and N. Ramakrishnan, Biophysical Journal **114**(8), 1830-1840 (2018) https://doi.org/10.1016/j.bpj.2018.03.007.

[15] Z. Jabeen, H. Y. Yu, D. M. Eckmann, P. S. Ayyaswamy, and R. Radhakrishnan, Phys. Rev. E **98**, 042602 (2018) https://doi.org/10.1103/PhysRevE.98.042602.

[16] M. Bishop and J. P. J. Michels, The Journal of Chemical Physics **85**(10), 5961-5962 (1986) http://dx.doi.org/10.1063/1.451508.

[17] J. Carlsson and J. Åqvist, The Journal of Physical Chemistry B **109**(13), 6448-6456 (2005) http://dx.doi.org/10.1021/jp046022f.

[18] M. A. Balsera, W. Wriggers, Y. Oono, and K. Schulten, The Journal of Physical Chemistry **100**(7), 2567-2572 (1996) http://dx.doi.org/10.1021/jp9536920.

[19] J. Li, S. Yu, P. Yao, and M. Jiang, Langmuir **24**(7), 3486-3492 (2008) http://dx.doi.org/10.1021/la702785b.

[20] A. J. Calderon, V. R. Muzykantov, S. Muro, and D. M. Eckmann, Biorheology **46**(4), 323-341 (2009) http://dx.doi.org/10.3233/BIR-2009-0544.

[21] M. C. Coll Ferrer, V. V. Shuvaev, B. J. Zern, R. J. Composto, V. R. Muzykantov, and D. M. Eckmann, One **9**(7), e10232 (2014) https://doi.org/10.1371/journal.pone.0102329.

[22] A. Ranganathan, J. Campo, J. Myerson, V. Shuvaev, B. Zern, V. R. Muzykantov, and D. M. Eckmann, Journal of Biomedical Nanotechnology **13**(6), 737-745 (2017) https://doi.org/10.1166/jbn.2017.2392.

[23] M. G. Davies and P. O. Hagen, Ann. Surg. **218**, 593-609 (1993).